Proposal for a solid-state magnetoresistive Larmor quantum clock

Amal Mathew [1], Kerem Y. Camsari [2], and Bhaskaran Muralidharan [3,*]

[1]*Department of Physics, Indian Institute of Technology Bombay, Powai, Mumbai 400076, India*

[2]*Department of Electrical and Computer Engineering, University of California, Santa Barbara, Santa Barbara, California 93106, USA*

[3]*Department of Electrical Engineering, Indian Institute of Technology Bombay, Powai, Mumbai 400076, India*

(Received 13 December 2021; revised 24 March 2022; accepted 28 March 2022; published 13 April 2022)

We propose a solid-state implementation of the Larmor clock that exploits tunnel magnetoresistance to distill information on how long itinerant spins take to traverse a barrier embedded in it. Keeping in mind that the tunneling time innately involves pristine preselection and postselection, our proposal takes into account the detrimental aspects of multiple reflections by incorporating multiple contacts, multiple current measurements, and suitably defined magnetoresistance signals. Our analysis provides a direct mapping between the magnetoresistance signals and the tunneling times and aligns well with the interpretation in terms of generalized quantum measurements and quantum weak values. By means of an engineered preselection in one of the ferromagnetic contacts, we also elucidate how one can make the measurement "weak" by minimizing the backaction, whereas keeping the tunneling time unchanged. We then analyze the resulting interpretations of the tunneling time and the measurement backaction in the presence of phase breaking effects that are intrinsic to solid-state systems. We unravel that whereas the time-keeping aspect of the Larmor clock is reasonably undeterred due to momentum and phase relaxation processes, it degrades significantly in the presence of spin dephasing. We believe that the ideas presented here also open up a fructuous solid-state platform to encompass emerging ideas in quantum technology, such as quantum weak values and its applications that are currently exclusive to quantum optics and cold atoms.

DOI: 10.1103/PhysRevB.105.144418

I. INTRODUCTION

Despite the lack of a "time operator" in quantum mechanics [1], quantum time keeping can be connected with the measurement of space-time distances [2–4] signifying the passage of time needed for a quantum process to occur, most generally, between two spatial coordinates [2,3]. The tunneling time—the time a particle takes to tunnel through a barrier that has been a subject at the heart of hot debates in physics [5–9] precisely fits into this paradigm. Büttiker and Landauer [10] and Büttiker [11], following earlier works [12–14], solidified a construct—the Larmor clock to estimate the tunneling time, which is based on the Larmor precession of a stream of spins inside a barrier subject to a weak Zeeman field perpendicular to the plane of the precession. This idea was further elegantly interpreted in the perspective of generalized von Neumann measurements [15] with the tunneling time proportional to a quantum weak value [4,16–21]. A holistic viewpoint of the tunnel time problem requires delving into the following intertwined aspects: (a) the construct of the Larmor clock that is based on a straightforward analysis of spin-dependent tunneling [11], the description of the tunneling time, and the dwell time from this analysis, (b) its connection with generalized von Neumann measurements in relation to a generic description of quantum time keeping, and (c) that the preselection and postselection of quantum states are inherently involved which necessitates a connection to quantum weak values [15].

Recent ground breaking experiments on this topic using a cold atoms realization of the Larmor clock [22,23] open the possibility of making the time-keeping aspects as well as the aspects related to quantum weak values accessible to a larger class of experiments. Given the current progress in nanoelectronics, and especially nanomagnetism and spintronics [24–26], a suitably designed solid-state device platform can potentially provide for a fruitful test bed to integrate such emerging ideas into such a platform. The object of this paper is to propose a prototype solid-state spintronic test bed that caters to the holistic viewpoint of quantum time keeping described above. We also believe that the ideas presented here can encompass emerging ideas in quantum technology, such as quantum weak values and its applications that are currently exclusive to quantum optics and cold atoms [21].

Before delving into our setup, we briefly describe the generics of quantum time keeping in connection with the Larmor clock, for which, we refer to Figs. 1(a) and 1(b). The measurement of tunnel time can be thought of in terms of a pointer that gets "kicked" as the particle tunnels through the barrier. The difference between the initial and the final pointer readings can be used to decipher the time taken for the process. In the Larmor clock, as depicted in Fig. 1(b), the spin orientation of the particle along the x-y plane acts as the pointer, and the in-plane angle of rotation denotes the pointer reading. Based on this, for the in-plane rotation to act as a viable pointer it becomes crucial to have a well-defined preselection and postselection [4,15] of states at the incident and at the transmitted regions, respectively.

Our proposal is schematized in Fig. 1(c) in which we utilize tunnel magnetoresistance transport signals to distill the

*bm@ee.iitb.ac.in

 ©2022 American Physical Society

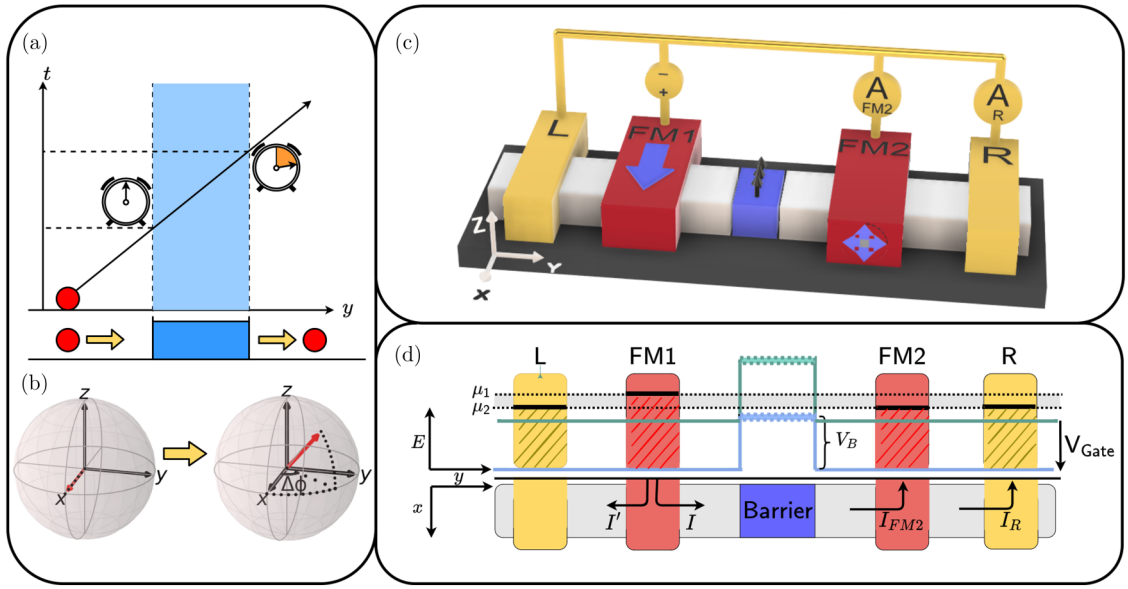

FIG. 1. Schematics: (a) Depiction of quantum time keeping in terms of tunneling time estimation. A pointer movement attached with the particle tracks the time taken. (b) A schematic of Larmor precession as well as the alignment in the $\hat{z}$ direction of a tunneling electron. (c) The proposed magnetoresistive setup. The yellow contacts are normal metallic (NM) contacts whereas the red contacts are ferromagnetic (FM) in the direction specified by the blue arrows. The current measurements across the two ammeters are used to deduce the necessary transport signals. The schematic is along the transport direction, $\hat{y}$, direction. (d) Because tunneling time is defined for a particular value of k, we consider a low-bias situation in which only electrons within a small energy range conduct current. The corresponding k values can be modulated by using a gate voltage to scan through the k space.

necessary information on the tunneling time of itinerant spins traversing a barrier embedded in it. Ferromangetic contacts take into account the crucial aspects involving the preselection and the postselective measurement. Unlike the cold atoms implementation, however, spintronic devices suffer from setbacks, such as multiple reflections at the ferromagnetic contacts, impurities, and channel phase breaking processes. These aspects are serious impediments specifically to preselection and postselection of the states that the proposal heavily relies on. The detrimental aspect of multiple reflections, we show, can be mitigated using additional "padding contacts" and incorporating multiple current measurements that will be described in detail.

Using the Keldysh nonequilibrium Green's function (NEGF) technique [27–29] to calculate the transport signals, we first demonstrate that our analysis provides a direct mapping between the magnetoresistance signals and the Larmor tunneling times. Our results also consistently align with the interpretation of the tunneling time as a quantum weak value with the real and imaginary parts signifying the tunneling time and the measurement backaction [15,21]. By means of an engineered preselection in one of the ferromagnetic contacts, we further elucidate how one can make the measurement "weak" by minimizing the backaction, whereas keeping the tunneling time unchanged.

We further analyze the resulting interpretations of the tunneling time and the measurement backaction in the presence of phase breaking effects [27,30–37], that are intrinsic to solid-state systems. We uncover that, whereas the time-keeping aspect of the Larmor clock is reasonably undeterred due to momentum and phase relaxation processes, it degrades significantly in the presence of spin dephasing.

The paper is organized as follows. In Sec. II, we formalize the crucial aspects that were described earlier before describing the magnetoresistive setup in detail in Sec. II C. The results are expanded in Sec. III. In Sec. III A, we show the central results of the proposal wherein the magnetoresistive Larmor clock setup matches the theoretical framework from earlier works. In Sec. III B, we explore the aspect of minimizing the measurement backaction. In Sec. III C, we demonstrate the effects of dephasing on the time-keeping aspect of our proposed setup. We conclude in Sec. IV.

II. DEVICE SETUP

A. The Larmor clock

For the orientation we consider, $\hat{x}$-polarized spins tunnel through a barrier that encloses a Zeeman field in the $\hat{z}$ direction. Inside this barrier the spins undergo Larmor precession in the x-y plane and a damping that tries to orient the spins along the $\hat{z}$ direction. In the weak magnetic-field limit, the orientation of the average spin $\langle S\rangle$ of the outgoing stream dictates the tunnel time, which can be written as

$$\begin{aligned}\langle S_Z\rangle &= (\hbar/2)\omega_L\tau_Z,\\ \langle S_Y\rangle &= -(\hbar/2)\omega_L\tau_Y,\\ \langle S_X\rangle &= (\hbar/2)\big(1-\omega_L^2\tau_X^2/2\big),\end{aligned} \tag{1}$$

where $\hbar\omega_L/2$ is the Zeeman energy and ω_L is the Larmor frequency. Although τ_Y and τ_Z are purely mathematical constructs that describe various times involved in the tunneling process, Büttiker [11] argued that the actual tunneling time is given by $\tau_T = \sqrt{\tau_Y^2+\tau_Z^2}$. It was further remarked that τ_T is the tunneling traversal time and that in the case of symmet-

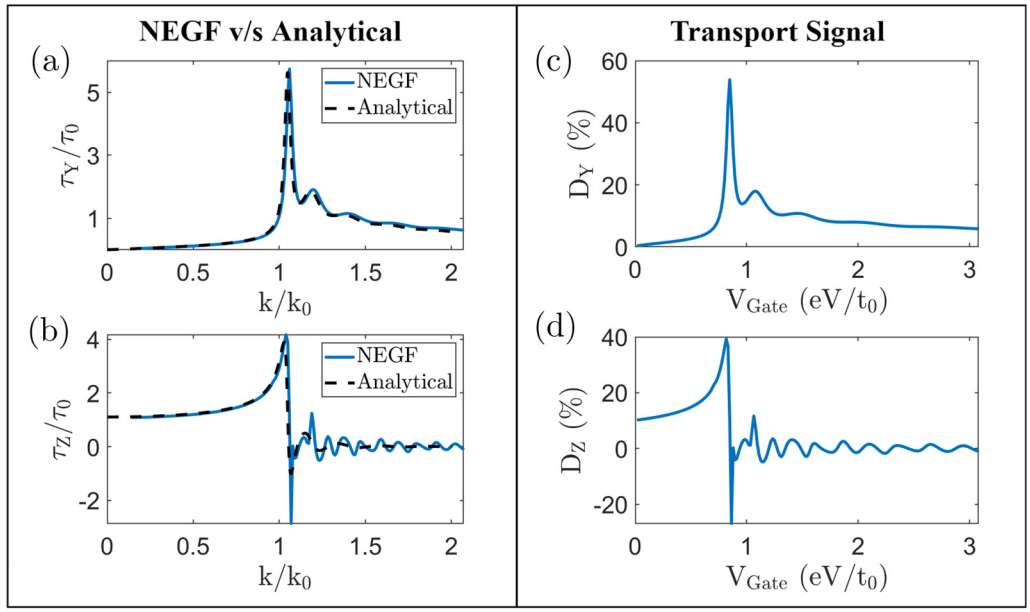

FIG. 2. Transport signals and comparison with the Büttiker model [11]. (a) Tunneling time and (b) measurement backaction as a function of k as predicted by NEGF model which matches the analytical results from the Büttiker model [11]. (c) and (d) The corresponding magnetoresistive transport signal D_Y and D_Z, respectively. For our setup, measurable polarization in percentages gives the embedded information on τ_Y and τ_Z as seen in (a) and (b).

ric barriers, such as the ones considered here, it is equal to another quantity called the dwell time τ_d. Keeping in mind various stimulating discussions in this field, we will follow the interpretation based on generalized measurements [15].

B. Generalized measurements

To formalize the above discussion, we refer back to the schematic in Fig. 1(a), which depicts the space-time measurement. Connecting with the theory of generalized measurements discussed in Appendix C, the $\hat{S}_z$ operator is the generator of the Larmor precession angle $\hat{\phi}$ for measuring the spatial barrier operator $\hat{U}(y)$. The interaction Hamiltonian that defines the measurement process is then given by $\hat{H}_{\rm int} = g\mu_B B_z \hat{S}_z \hat{U}(\hat{y})$, which represents the standard Zeeman interaction Hamiltonian with a magnetic-field B_z along the $\hat{z}$ direction, but only limited to the barrier region represented by the barrier function $\hat{V}(\hat{y})$. Connecting with the Büttiker clock, the stream of $\hat{x}$-polarized electrons form the preselection and the measurement along $\hat{y}$ or $\hat{z}$ direction forms the postselection process.

Quantum weak values. Whereas the treatment of the Larmor clock gives a straightforward prescription for calculating $\tau_{Y(Z)}$, it can be established that τ_Y and τ_Z from (1) actually translate to the real and imaginary parts of the weak value of the measurement process described above and is defined as

$$\tau_Y = \frac{m}{\hbar k}\mathbf{Re}\left(\frac{\langle f|\hat{U}(\hat{y})\mid i\rangle}{\langle f\mid i\rangle}\right), \tag{2}$$

$$\tau_Z = \frac{m}{\hbar k}\mathbf{Im}\left(\frac{\langle f\mid \hat{U}(\hat{y})\mid i\rangle}{\langle f\mid i\rangle}\right), \tag{3}$$

where $\langle y|i(f)\rangle$ represents the wave function of the incident (transmitted) stream of spins. The incident and the transmitted beams represent the preselection and the postselection, respectively. The weak value has both real and imaginary components and, thus, in this interpretation, τ_Y alone is the tunneling time, whereas τ_Z, the imaginary part represents the backaction due to the measurement process.

C. Magnetoresistive setup

Consolidating the concepts discussed above and elaborated in Appendix C, we now proceed to a detailed exposition of the magnetoresistive setup, shown in Fig. 1(c). The device region consists of a long enough single moded channel with a barrier in the middle where a small Zeeman field B_z is applied along the $\hat{z}$ direction with the Zeeman splitting energy V_Z. Two NM contacts are placed at the ends in order to manipulate reflections and, hence, produce a viable transport signal at the ammeters. The ferromagnetic (FM1) contact on the left side injects the $\hat{x}$-polarized stream of electrons, and the ferromagnetic contact (FM2) on the right side is used as the detector for postselective measurement, whose orientation is along the $\hat{y}$ direction or the $\hat{z}$ direction, so as to measure τ_Y or τ_Z, respectively. The unpolarized contact to the left of FM1 acts as a sink that collects the reflected waves from the barrier. We read the currents through the $\pm\hat{y}$- (or $\pm\hat{z}$-) polarized FM2 contacts which are also grounded. Since the current drains into these contacts, and they are located "downstream" from the barrier, postselection rules are also satisfied, and the measured current is composed of electrons that have tunneled through the barrier.

The entire setup is backgated such that a gate voltage V_G can add an energy offset to the entire channel in order to select a particular carrier momentum k. Figure 1(d) shows the schematic of the cross section of the setup with the two NM contacts kept at electrochemical potentials μ_1 and μ_2. For the transport measurement, a small electrochemical potential dif-

ference $\mu_1 - \mu_2 = eV$ is maintained such that a small applied voltage can inject the desired momentum k for the incoming stream of electrons.

Transport signals. Following a detailed analysis (see Appendix B) of multiple reflections at the FM contacts, we can show that the transport signal D_Y related to τ_Y can be derived based on the currents registered at the FM2 contact,

$$D_Y = \frac{I^+_{FM2} - I^-_{FM2}}{I^+_{FM2} + I^-_{FM2}}, \tag{4}$$

where I^+_{FM2} and I^-_{FM2} represent the measured currents at the FM2 contact when it is polarized in the $+\hat{y}$ and $-\hat{y}$ directions, respectively. This transport signal D_Y is a measure of polarization of $\hat{y}$ spin of electrons in the channel. Specifically, we have the average postselected $\hat{y}$ component of the spin as

$$\langle S_Y \rangle = (\hbar/2)\frac{I^+_{FM2} - I^-_{FM2}}{I^+_{FM2} + I^-_{FM2}} = -(\hbar/2)\omega_L \tau_Y. \tag{5}$$

We can, therefore, write the tunneling time τ_Y in terms of currents observed at the FM2 contact as

$$\tau_Y = -\frac{1}{\omega_L}\frac{I^+_{FM2} - I^-_{FM2}}{I^+_{FM2} + I^-_{FM2}}. \tag{6}$$

The derivation of the transport signature D_Z that captures the measurement backaction τ_Z as explained in Appendix B is more involved and is given by

$$D_Z = -\frac{(I^+_R - I^+_{FM2}) - (I^-_R - I^-_{FM2})}{(I^+_R - I^+_{FM2}) + (I^-_R - I^-_{FM2})}, \tag{7}$$

where $I^\pm_{FM2}$ are similar to the previous case, the currents through the FM2 contact whereas it is in the $\pm\hat{z}$ orientation, respectively. $I^\pm_R$ are the currents measured in the second ammeter connected to the right NM contact when the ferromagnetic contact is in the $\pm\hat{z}$ orientation, respectively. Thus, D_Z is analogous to D_Y defined in (4) and, correspondingly, measures the postselected $\hat{z}$ spin which is given by

$$\langle S_Z \rangle = -(\hbar/2)\frac{(I^+_R - I^+_{FM2}) - (I^-_R - I^-_{FM2})}{(I^+_R - I^+_{FM2}) + (I^-_R - I^-_{FM2})} = (\hbar/2)\omega_L \tau_Z. \tag{8}$$

Thus, the measurement backaction in terms of contact currents is given by

$$\tau_Z = -\frac{1}{\omega_L}\frac{(I^+_R - I^+_{FM2}) - (I^-_R - I^-_{FM2})}{(I^+_R - I^+_{FM2}) + (I^-_R - I^-_{FM2})}. \tag{9}$$

III. RESULTS

A. Coherent transport

With the above formulation, we evaluate the transport signal currents using the Keldysh NEGF technique [27,28] detailed in Appendix A. With the terminal current operator $\hat{I}^\alpha_{op}$, where $\alpha = FM1, FM2$, we can find quantities related to spin currents as $I^s_\alpha = \mathbf{Tr}[\hat{\sigma}\hat{I}_\alpha]$, where $\hat{\sigma}$ represents the vector Pauli spin operator. The channel is written in the tight-binding representation of the one-band effective-mass Hamiltonian with an on-site energy E_0 and hopping energy t_0. The barrier region in the middle has a potential V_B and is subject to a

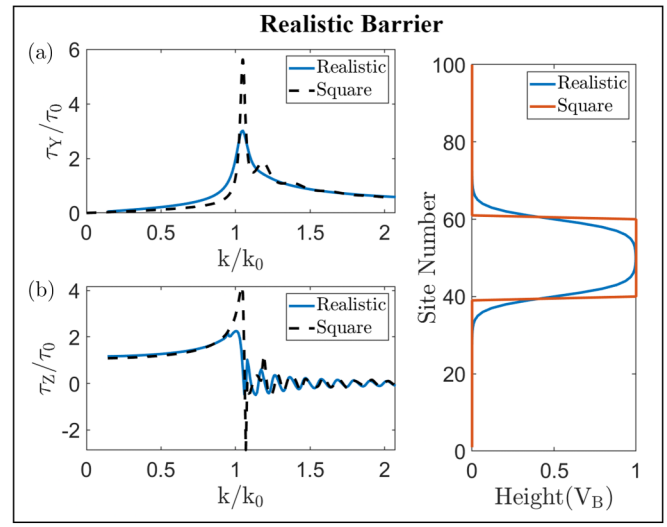

FIG. 3. Realistic barrier. (a) The tunnel time, and (b) measurement backaction profile as a function of carrier momentum k for a realistic barrier with band-bending effects. We clearly note the effect of the barrier narrowing near the top of the barrier and widening near the bottom.

Zeeman energy V_Z along the $\hat{z}$ direction. In order to resolve carrier momenta, we relate the energy of the carrier with the gate potential given by

$$E = -eV_G + 2t_0[1 - \cos(ka)]. \tag{10}$$

Assuming $E = 0$ without loss of generality such that the gate potential gives the required energy translation, gives the necessary transformation between carrier momenta and gate potential.

We observe that in the coherent ballistic regime, the results from our simulation are a near perfect match with the analytical results derived by Büttiker [11] as shown in Fig. 2. Figures 2(c) and 2(d) show the magnetoresistance signature D_Y as a function of the gate voltage, thus, correlating a magnetoresistance measurement with the Larmor tunnel time. We clearly see how an experimental setup that tracks the transport signals D_Y and D_Z that can indeed yield the tunneling time as well as a measure of the backaction. This aspect constitutes the crux of our solid-state Larmor clock.

Having demonstrated the setup in terms of reproducing transport signals that connect to the free-space Büttiker proposal [11], we move on to analyze a few realistic effects. First, we see what happens with realistic barriers and then move on to effects that relate to dephasing that naturally occurs in such solid-state setups.

Realistic barriers. Instead of a perfectly rectangular barrier, we now consider a barrier of the form

$$U(y) = V_B[\tanh(L/2 - y) + \tanh(L/2 + y)]/2. \tag{11}$$

This is implemented by replacing the perfect square barrier potential in the channel Hamiltonian by a the appropriate function defined above.

As noted in Fig. 3, we find that for such a barrier, in the tunneling regime, i.e., $k/k_0 < 1$, where $k_0 = \sqrt{2mV_B}/\hbar$, electrons take a longer time to traverse the barrier. However, the maxima

of the tunneling time is smaller than that of the rectangular barrier. This is expected since the barrier has indeed thinned near the top as expected in a typical band-bending situation created upon contacting dissimilar materials. We also note that the tunneling time is greater at smaller energies due to the widening of the barrier in those regions.

B. Minimizing the measurement backaction

We now focus on the interpretation of the imaginary part τ_Z that relates to the measurement backaction. According to Steinberg [15], it possible to make this measurement "weaker" and reduce the measurement backaction by preparing the electron in a spin-squeezed initial state that increases the uncertainty in the pointer position. Although squeezed states are impossible to prepare from a solid-state perspective, we present an alternate method that can exhibit similar phenomena. This aspect is elaborated in Appendix D. We consider injected electrons with its spin oriented on the x-z plane as opposed to the $\hat{x}$ orientation considered earlier. This can be carried out by using external magnetic fields to rotate the ferromagnetic contacts as commonly performed in spintronic experiments to modulate the injection and detection (pre-/postselection) of spins [38]. This decreases the uncertainty in S_Z and increases the uncertainty in the pointer $\hat{\phi}$ position. We have from Ref. [15] that the change in pointer position (corresponding to τ_Y) and the pointer momentum (corresponding to τ_Z) is related to the uncertainty in pointer position as

$$\begin{aligned} \Delta\phi &= \omega_L \tau_Y = k\,\mathrm{Re}\langle U(y)\rangle_{fi}, \\ \Delta S_Z &= \omega_L \tau_Z = k\,\mathrm{Im}\langle U(y)\rangle_{fi}/2\sigma^2, \end{aligned} \tag{12}$$

where $\langle U(y)\rangle_{fi}$ is the weak value of the barrier function $U(y)$, σ^2 is the variance in the ϕ distribution. This implies that the precession angle remains constant whereas the measurement backaction decreases proportional to a decrease in uncertainty in S_Z. This is explicitly verified using our calculations on our setup where on comparing Figs. 4(a) and 4(b), we clearly note the measurement backaction decreasing as the variance in S_Z decreases, whereas keeping the signal pointer position $\Delta\phi$ unchanged. This implies clearly that the measured tunnel time is indeed τ_Y, thus, complying with the interpretation in Ref. [15].

C. Channels with dephasing

Dephasing interactions that are typical in solid-state systems, typically give rise to phase breaking processes that would degrade the crucial phase coherent nature of the spins. Typical interactions of this kind include pure phase relaxation via electron-electron interactions, momentum, and phase relaxation via fluctuating local nonmagnetic impurities and spin relaxation via magnetic impurities. These aspects can be added phenomenologically within the framework of the Keldysh NEGF formalism [27,30–32,35–37] via appropriate dephasing self-energies.

Phase as well as momentum relaxation processes [39] within the channel can be added via a scattering self-energy and its related in-scattering self-energy [36] in its matrix form

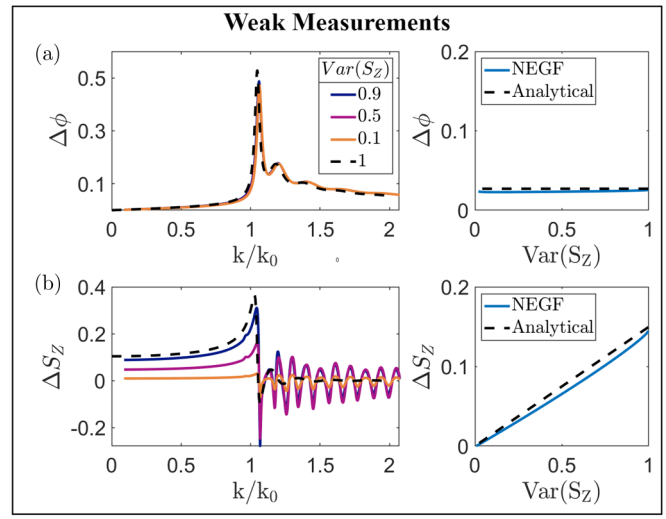

FIG. 4. Minimizing the measurement backaction. (a) Precession angle of electron spin about the $\hat{z}$ axis ($\Delta\phi$) is found to remain constant whereas (b) the measurement backaction, ΔS_Z decreases proportional to the variance in S_Z, indicating that the pointer deflection is unaffected. This aligns well with Ref. [15] (see the corresponding right insets for results at $k = 0.8k_0$) that the tunnel time is indeed τ_Y, which remains constant as the measurement is made weaker.

as

$$\begin{aligned} \left[\boldsymbol{\Sigma}_s^r\right]_{ij} &= D_{ijkl}[\mathbf{G}^r]_{kl}, \\ \left[\boldsymbol{\Sigma}_s^<\right]_{ij} &= D_{ijkl}[\mathbf{G}^<]_{kl}, \end{aligned} \tag{13}$$

where D_{ijkl} is an appropriate tensor that comprises the spatial correlation between the impurity scattering potentials [36]. The quantities $[\mathbf{G}^r]_{kl}$, $[\mathbf{G}^<]_{kl}$ represent the retarded Green's function and the lesser Green's function in the matrix representation, respectively. For pure-phase dephasing interactions where only the phase is relaxed, this tensor has the form

$$D_{ijkl} = D_P \delta_{ik}\delta_{jl} \tag{14}$$

where D_P is a tunable parameter that controls the strength of the interactions and δ_{ij} is the Kronecker δ function. For momentum dephasing in which the phase is inevitably relaxed [27], the corresponding tensor for these interactions is given by

$$D_{ijkl} = D_M \delta_{ij}\delta_{ik}\delta_{jl}, \tag{15}$$

where D_M is the corresponding tunable parameter. In our paper, this effect is termed as "phase + momentum" relaxation and it indeed corresponds to disorder averaging of local nonmagnetic impurity potentials [40,41].

In the presence of such interactions, the observed tunneling time profile is altered as shown in Fig. 5. Note that both these interactions preserve the spin of the electron and, therefore, do not affect the measurement mechanism of the setup, which relates to the pointer movement. Thus, all the deviations from coherent tunneling time as observed in Fig. 5 indicate disturbances in the actual tunneling process. We note that in the presence of pure-phase relaxing interactions, there is an observed broadening in the tunnel time profile. It is also noted

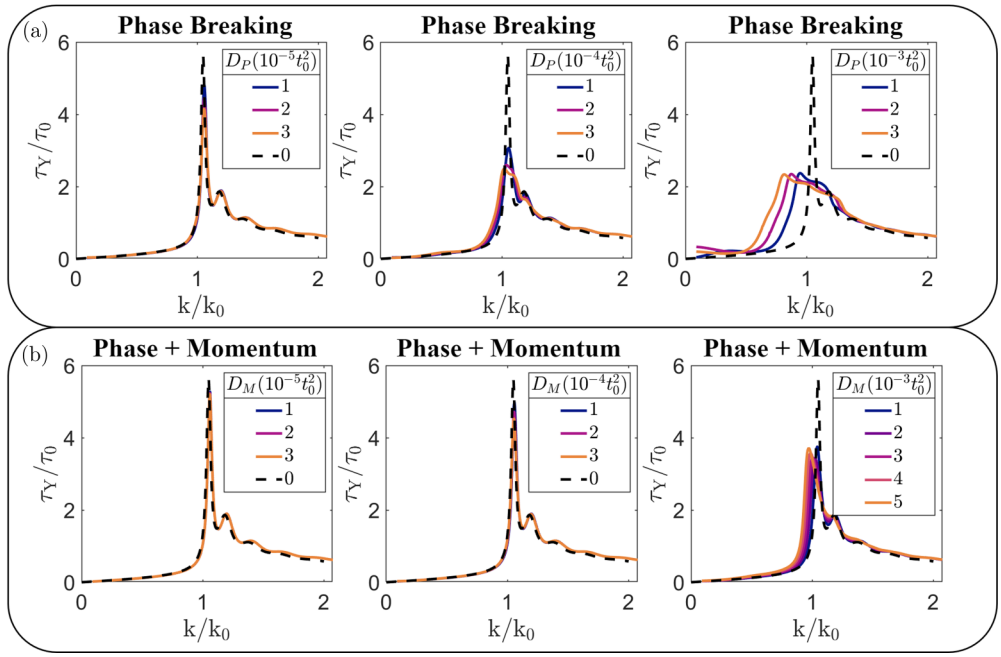

FIG. 5. Effect of phase relaxation and momentum relaxation. Tunnel time τ_Y profiles for varying strengths of the dephasing interaction parameter for (a) pure phase relaxation and (b) for momentum relaxation interactions. Note that the dephasing interactions in (a) and (b) are spin preserving and the observed disturbance in the transport signal is purely a result of disturbance in the tunneling phenomenon itself.

that increasing the strength of interactions decreases the tunnel time for electrons with energies close to the height of the barrier. In the presence of momentum relaxing interactions, however, whereas this effect is less pronounced, a shift in the peak of the function can be observed towards lower energies. This seems to suggest that introducing momentum dephasing interactions to the system lowers the perceived height of the barrier for the electron, consistent with the band-tail effects [40] that occur due to momentum relaxation processes.

Note that in the case of pure-phase relaxation, the self-energy matrix modifies the *entire* electron density matrix $G^n = -iG^<$, whereas in the case of phase + momentum relaxation, the self-energy matrix only modifies the block-diagonal portion of G^n. This means that the strength of dephasing (measured in t_0^2) in these two cases are not of one-to-one correspondence and they result in both qualitative and quantitative modifications to the line shape of the signal.

We now study the effect of spin relaxation interactions or equivalently spin dephasing [42] which can be included via

$$\begin{aligned}\left[\boldsymbol{\Sigma}_s^r\right]_{ij} &= D_S\left(\boldsymbol{\sigma}_x \mathbf{G}_{i,j}^r \boldsymbol{\sigma}_x + \boldsymbol{\sigma}_y \mathbf{G}_{i,j}^r \boldsymbol{\sigma}_y + \boldsymbol{\sigma}_z \mathbf{G}_{i,j}^r \boldsymbol{\sigma}_z\right),\\ [\boldsymbol{\Sigma}_s^<]_{ij} &= D_S(\boldsymbol{\sigma}_x \mathbf{G}_{i,j}^< \boldsymbol{\sigma}_x + \boldsymbol{\sigma}_y \mathbf{G}_{i,j}^< \boldsymbol{\sigma}_y + \boldsymbol{\sigma}_z \mathbf{G}_{i,j}^< \boldsymbol{\sigma}_z),\end{aligned} \tag{16}$$

where $\boldsymbol{\sigma}_i$ are the Pauli matrices and $\mathbf{G}_{i,j}^r$ and $\mathbf{G}_{i,j}^<$ correspond to the diagonal 2×2 sub-blocks of the matrix representation of the retarded Green's function and lesser Green's function, respectively. This form of the self-energy matrix serves the purpose of re-injecting electrons of opposite spin into the channel thereby relaxing spin. The observed tunnel time in this scenario is altered as shown in Fig. 6. Note that even at very small values of dephasing, the tunnel time signal is completely lost. This agrees with the fact that introducing spin-relaxing processes in the system destroys the measurement setup by randomizing the "pointer apparatus" itself. Thus, we note that the time-keeping mechanism for tunnel time and the associated weak values break down in the presence of spin dephasing, whereas it remains intact, albeit measuring an altered tunnel time when subject to moderate phase and momentum relaxation. These results are also consistent with the signals obtained for τ_Z (backaction) in

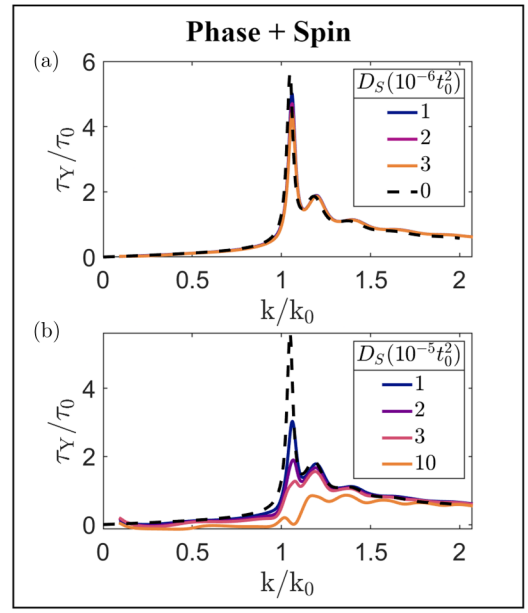

FIG. 6. Effect of spin relaxation on the tunnel time profile. (a) For very small values of dephasing parameter we notice some preservation of the tunneling time profile. (b) However, as the dephasing parameter is increased even marginally, we note a complete breakdown of the tunnel time profile.

the presence of dephasing interactions. They are qualitatively similar and reaffirm our understanding of tunneling time in the presence of dephasing

Feasibility of the setup. The Larmor clock signal in our setup is fairly robust against phase and momentum dephasings in the channel. This relaxes the practically difficult requirement of designing phase-coherent ballistic channels. However, the signal is particularly sensitive to spin dephasing (Fig. 6). Spin dephasing occurs in a quantum channel due to various contributing mechanisms, which culminate in the experimentally accessible spin-diffusion length parameter. In clean channels without any magnetic impurities and little spin-orbit coupling (such as silicon) it is experimentally well established that the spin-diffusion lengths can be of the order of tens of micrometers (see, for example, Refs. [43,44]). As such, we believe that the Larmor signal can be observed in such quantum channels.

IV. CONCLUSION

In this paper, we proposed a solid-state implementation of the Larmor clock that exploits tunnel magnetoresistance to distill information on how long the itinerant spins take to traverse a barrier embedded in it. In the coherent transport limit, our analysis provided a direct mapping between the magnetoresistance signals and the tunneling times, thereby aligning with the well-known interpretation of the tunneling time as a quantum weak value. By means of an engineered preselection in one of the ferromagnetic contacts, we also elucidated how one can make the measurement weak by minimizing the backaction, whereas keeping the tunneling time unchanged. We then analyzed the resulting interpretations of the tunneling time and the measurement backaction in the presence of phase breaking effects [27,30–37] intrinsic to solid-state systems. It is clearly demonstrated that, whereas the time-keeping aspect of the Larmor clock is reasonably undeterred due to momentum and phase relaxation processes, it degrades significantly in the presence of spin dephasing. We believe that the ideas presented here can potentially open up a fertile solid-state spintronics platform to encompass emerging ideas in quantum technology, such as quantum weak values and its applications that are currently exclusive to quantum optics and cold atoms. Whereas the setup we describe provides a basic realization of a spintronic Büttiker clock consistent with the interpretations of Steinberg [15], it is left further to look into the thermodynamic aspects of quantum time keeping via a serious analysis of pointer tick accuracy and efficiency [45–47]. Mesoscopic quantum Hall setups with quantum point contacts also possess realizable configurations for delving deep into these aspects discussed here. Furthermore, the interaction with nuclear spins via the hyperfine interaction can offer new insights into continuous weak measurements [48–50]. Another avenue of interest is the study of such systems in the presence of spin-orbit coupling (SOC), for example, in a setup where there is SOC within the tunnel barrier, the SOC interactions in the barrier could then act as an effective magnetic field, the measurement of which could give us an idea of the strength of spin-orbit interactions in the material. Ideas similar to this have been explored in the context of spin transistors (Datta-Das [51]) and could potentially be important to analyze in our setup as well. Most importantly, the general problem of space-time distance estimation in quantum systems is still a matter of intense pursuit and conceptual advancement where relativistic quantum time dilation may also be possible [52], and suitable test beds may be built featuring quantum materials.

ACKNOWLEDGMENTS

We wish to acknowledge S. Datta, S. Vinjanampathy, and A. Tulapurkar for useful discussions. The research and development work undertaken in the project under the Visvesvaraya Ph.D Scheme of the Ministry of Electronics and Information Technology (MEITY), Government of India, was implemented by Digital India Corporation (formerly Media Laboratory Asia). This work was also supported by the Science and Engineering Research Board (SERB), Government of India, Grant No. STR/2019/000030, the Ministry of Human Resource Development (MHRD), Government of India, Grant No. STARS/APR2019/NS/226/FS under the STARS scheme.

APPENDIX A: THE KELDYSH NONEQUILIBRIUM GREEN'S FUNCTION TECHNIQUE

The Keldysh NEGF method [27,29] can be used to set up a systematic framework to evaluate the required currents and other quantities. In our formulation of the Keldysh NEGF, the device is connected with multiple leads. First, we consider a channel described by a standard tight-binding Hamiltonian of the form

$$H = E_0 - t_0 \sum_{i,\sigma} (c^{\dagger}_{i\sigma} c_{i+1,\sigma} + \text{H.c.}), \tag{A1}$$

where $i \in \{1, N\}$ is the lattice index, $\sigma \in \{-1, 1\}$ is the spin index, and H.c., stands for the Hermitian conjugate. In the matrix form, this is given by a $2N \times 2N$ matrix with $E_0 I_{2\times 2}$ on the 2×2 block diagonals and $-t_0 I_{2\times 2}$ on the 2×2 upper and lower off-diagonals.

We then add a barrier with an enclosed magnetic field in the $\hat{z}$ direction to the channel which has the form

$$U(y) = \left(V_B I - \frac{V_Z \sigma_z}{2}\right)\left[\Theta\left(y - \frac{N}{2} + \frac{L}{2}\right) - \Theta\left(y - \frac{N}{2} - \frac{L}{2}\right)\right], \tag{A2}$$

where V_B is the barrier potential, I is the 2×2 identity matrix, V_Z is the Zeeman splitting energy in the $\hat{z}$ direction, σ_z is the Pauli matrix in $\hat{z}$, $\Theta(x)$ is the Heaviside step function, L is the length of the barrier, and N is the length of the channel. The matrix form

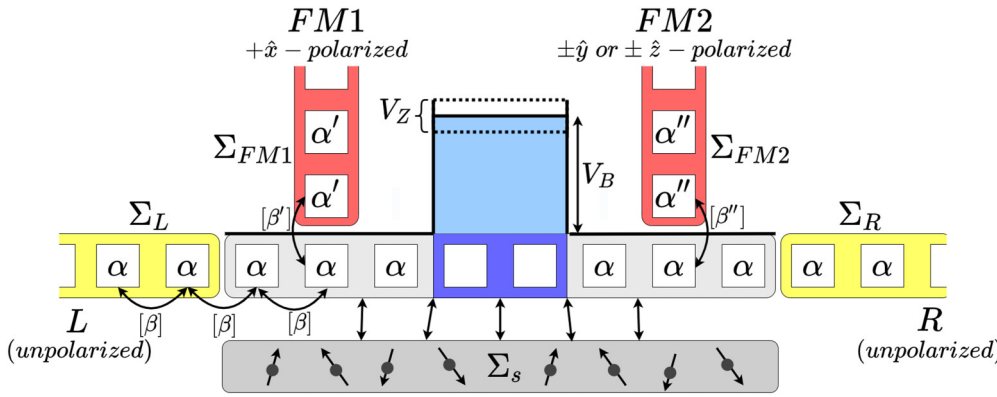

FIG. 7. Schematic of the lattice structure of the setup along with a depiction of the contact self-energies as well as the dephasing self-energy as used in the NEGF method. α, β are the on-site and hopping elements in the channel Hamiltonian. Unpolarized contacts (yellow) and polarized contacts (red) are accounted for via the respective self-energies. The scatterers that are responsible for dephasing are represented via another bath and are accounted for via an additional self-energy.

of the above potential is simply given by

$$U_{ij} = \begin{cases} (V_B I_{2\times 2} - V_Z \sigma_z/2)\delta_{ij} & \text{for } N/2 - L/2 \leqslant i \leqslant N/2 - L/2, \\ 0, & \text{otherwise,} \end{cases} \tag{A3}$$

where U_{ij} represents the 2×2 block at location (ij) in the matrix. A schematic of the device simulation setup has been sketched in Fig. 7.

Now from the device Hamiltonian H, and using (A3), (A5), and (A7), the retarded Green's function G^r can be obtained as

$$G^r = \left[EI - H - U - \Sigma_c^r - \Sigma_s^r\right]^{-1}, \tag{A4}$$

where $\Sigma_c^r = \sum_\alpha \Sigma_\alpha^r$ is the sum of all the contact retarded self-energies associated with contacts labeled α, where $\alpha = FM1, FM2, L, R$, and Σ_s^r is the scattering self-energy used to model scattering interactions.

For an unpolarized contact, the retarded self-energy Σ_α^r attached to a point i in the channel has only two nonzero elements in its $2N \times 2N$ matrix form, given by $[\Sigma_\alpha^r]_{i,i} = -t_0 e^{ika} I_{2\times 2}$. Thus, the retarded self-energy matrices of the two unpolarized contacts in our channel Σ_L^r and Σ_R^r are given by

$$\begin{aligned} \left[\Sigma_L^r\right]_{i,j} &= -t_0 e^{ika} I_{2\times 2}\delta_{1,i}\delta_{1,j}, \\ \left[\Sigma_R^r\right]_{i,j} &= -t_0 e^{ika} I_{2\times 2}\delta_{N,i}\delta_{N,j}. \end{aligned} \tag{A5}$$

For a perfectly polarized ferromagnetic contact polarized in the $\hat{p}_\alpha$ direction and located at a point i in the channel, the self-energy matrix has a block diagonal form given by

$$\left[\Sigma_\alpha^r\right]_{ii} = -t_0 e^{ika}(I_{2\times 2} + \hat{\mathbf{p}}_\alpha \cdot \boldsymbol{\sigma})/2, \tag{A6}$$

where $\boldsymbol{\sigma}$ are the Pauli matrices.

Thus, the self-energy matrices of the two FM-polarized contacts in our channel Σ_{FM1}^r and Σ_{FM2}^r are given by

$$\begin{aligned} \left[\Sigma_{FM1}^r\right]_{i,j} &= -\frac{t_0 e^{ika}}{2}(I_{2\times 2} + \boldsymbol{\sigma}_x)\delta_{(N-L)/4,i}\,\delta_{(N-L)/4,j}, \\ \left[\Sigma_{FM2}^r\right]_{i,j} &= \begin{cases} -\frac{t_0 e^{ika}}{2}(I_{2\times 2} \pm \boldsymbol{\sigma}_y)\delta_{(3N+L)/4,i}\,\delta_{(3N+L)/4,j}, & \text{whereas measuring } \tau_Y, \\ -\frac{t_0 e^{ika}}{2}(I_{2\times 2} \pm \boldsymbol{\sigma}_z)\delta_{(3N+L)/4,i}\,\delta_{(3N+L)/4,j}, & \text{whereas measuring } \tau_Z. \end{cases} \end{aligned} \tag{A7}$$

The $FM1$ contact is located at position $(N - L)/4$ and the $FM2$ contact is located at position $(3N + L)/4$.

Now, the lesser self-energies of the contacts are given by

$$\Sigma_\alpha^< = i\Gamma_\alpha f_\alpha, \tag{A8}$$

where Γ_α is simply the broadening function given by the imaginary part of the self-energy, such that $\Gamma_\alpha = i[\Sigma_\alpha^r - \Sigma_\alpha^a]$ and f_m is the corresponding occupation factor.

Then, the lesser Green's function $G^<$ at a particular energy is given by

$$G^< = G^r\left[\Sigma_c^< + \Sigma_s^<\right]G^a, \tag{A9}$$

where $G^a = [G^r]^\dagger$ is the advanced Green's function, $\Sigma_c^< = \sum_\alpha \Sigma_\alpha^<$ is the sum of all contact lesser self-energies and $\Sigma_s^<$ is the lesser self-energy arising from the dephasing interactions. $G^n = -iG^<$ represents the electron density (times 2π) inside the channel.

The spectral function A is obtained as

$$A = i[G^r - G^a] = G^r[\Gamma_c + \Gamma_s]G^a. \tag{A10}$$

The diagonal elements of the spectral function are related to the local density of states at the corresponding lattice point in

the channel. We are now left with defining the scattering self-energies due to dephasing processes considered in this paper.

Dephasing self-energies. To account for scattering in the contacts, we introduce a self-energy matrix for the various dephasing processes [30,31]. We consider impurities with localized potentials $U_s(i)$ in the channel and use their correlator $\bar{D}(i,j) = \langle U_s(i)U_s^*(j)\rangle$ to calculate the self-energy of interaction processes. This facilitates a smooth transition from the ballistic regime to the diffusive regime.

The self-energy for the momentum dephasing process is given by

$$\Sigma_s^r(i,j) = \bar{D}(i,j)G^r(i,j), \tag{A11}$$

$$\Sigma_s^<(i,j) = \bar{D}(i,j)G^<(i,j), \tag{A12}$$

where $G^<(i,j)$ is the lesser Green's function and $\bar{D}(i,j)$ is given by

$$\bar{D}(i,j) = \langle U_s(i)U_s^*(j)\rangle, \tag{A13}$$

$$\bar{D}(i,j) = D_m\delta_{ij}. \tag{A14}$$

This model discards the off-diagonal elements of the Green's function, thus, relaxing both the phase and the momentum of quasiparticles in the channel. The quantity D_m is the dephasing parameter which represents the magnitude squared of the fluctuating scattering potentials. This parameter can be modulated so that by gradually increasing it, one can transition from the coherent ballistic limit to the diffusive limit.

Similarly, the self-energy for pure phase dephasing process is given by

$$\Sigma_s^r = \bar{D}_pG^r, \tag{A15}$$

$$\Sigma_s^< = \bar{D}_pG^<, \tag{A16}$$

where $\bar{D}_p$ is again the dephasing parameter that controls the magnitude of interactions. Here, the entire Green's function is preserved as the self-energy matrix and relaxes only the phase of the quasiparticles.

Spin-flip interactions can be added to the channel via the introduction of a corresponding self-energy of the form

$$\begin{aligned}\left[\boldsymbol{\Sigma}_s^r\right]_{ij} &= D_S\left(\boldsymbol{\sigma}_x\mathbf{G}_{i,j}^r\boldsymbol{\sigma}_x + \boldsymbol{\sigma}_y\mathbf{G}_{i,j}^r\boldsymbol{\sigma}_y + \boldsymbol{\sigma}_z\mathbf{G}_{i,j}^r\boldsymbol{\sigma}_z\right),\\ \left[\boldsymbol{\Sigma}_s^<\right]_{ij} &= D_S\left(\boldsymbol{\sigma}_x\mathbf{G}_{i,j}^<\boldsymbol{\sigma}_x + \boldsymbol{\sigma}_y\mathbf{G}_{i,j}^<\boldsymbol{\sigma}_y + \boldsymbol{\sigma}_z\mathbf{G}_{i,j}^<\boldsymbol{\sigma}_z\right).\end{aligned} \tag{A17}$$

The effect of this dephasing mechanism is to re-inject an electron with an opposite spin back to the channel that relaxes spin.

Current operator. The NEGF formalism provides us a clear-cut current operator that can be used to calculate all kinds of currents through a contact α, given by

$$\mathbf{I}_{\text{op}}^{\alpha} = \frac{1}{h}\left(\left[\boldsymbol{\Sigma}_{\alpha}^{\mathbf{r}}\mathbf{G}^< - \mathbf{G}^<\boldsymbol{\Sigma}_{\alpha}^a\right] + \left[\boldsymbol{\Sigma}_{\alpha}^<\mathbf{G}^a - \mathbf{G}^r\boldsymbol{\Sigma}_{\alpha}^<\right]\right), \tag{A18}$$

where the current of a particular quantity X is given by $I_X^{\alpha} = \text{Trace}(I_{op}^{\alpha}X_{op})$ To find the charge current through the contact, we then simply need to find $I_{\alpha} = \text{Trace}(I_{op}^{\alpha})$ since the charge operator is the identity matrix (times e). Then, the charge current per unit energy through a particular contact m, is given by

$$\tilde{I}_{\alpha} = \frac{-ie}{h}\,\text{Trace}\left[\Sigma_{\alpha}^<A - \Gamma_{\alpha}G^<\right]. \tag{A19}$$

In our setup, we measure the currents through the right unpolarized contact (R) as well as the right ferromagnetic contact (FM2), both of which are grounded.

Using (A9) solved self-consistently with the equations for the retarded Green's functions given in Eq. (A4) and self-energies given in (A5), (A7), (A14), and (A16), we next obtain the currents given by (A19). We then calculate the spin polarization in the channel using the currents through the respective contacts.

APPENDIX B: TRANSPORT SIGNALS FOR THE TUNNELING TIME AND THE BACKACTION

We refer to Figs. 8(a) and 8(b) for a description of the transport signal for τ_Y. In order to measure the dwell time of the electron, the average in-plane precession of the tunneled electron needs to be measured. In other the words, a weak value measurement of the σ_Y operator is required. To do this, we consider the right polarized contact in the $\pm\hat{y}$ directions. To understand this measurement, consider two spin channels in the device, carrying electrons of spin polarization $+\hat{y}$ and $-\hat{y}$. Electrons that are in a superposition of these states travel simultaneously through both channels. The presence of a $+\hat{y}$-polarized ferromagnetic contact then acts as a fork in the channel; with an electron in the $+\hat{y}$ channel draining into either the ferromagnetic $+\hat{y}$ contact, or the unpolarized contact. On the other hand, an electron in the $-\hat{y}$ channel can only drain into the unpolarized contact. In addition to this, the Zeeman field in the barrier, being in the $+\hat{z}$ direction, couples the wave functions in the two channels. Now, let the currents through the two channels, in the absence of any forks be given by α and β, respectively, for the $\pm\hat{y}$ channels. The presence of a fork in the $+\hat{y}$ channel then modifies the current through each of the forks to be $c_1\alpha$ where c_1 is some constant parameter (since the forks are identical). Note that this is independent of β since the wave function in the $-\hat{y}$ channel does not affect the current through the $+\hat{y}$ channel. However, the opposite is not true. The reflected wave function from the fork in the $+\hat{y}$ channel is coupled to the $-\hat{y}$ channel through the $+\hat{z}$ Zeeman field in the barrier. Thus, the current through this channel is given by $\beta + c_3\alpha$ where c_3 is some other constant parameter.

Then, in the presence of the ferromagnetic $+\hat{y}$-polarized contact, the currents through the two contacts are now given by $I_{FM2}^+ = c_1\alpha$ (for the $+\hat{y}$-polarized contact) and $I_R^+ = (c_1 + c_3)\alpha + \beta$ (for the unpolarized contact).

For the ferromagnetic contact polarized in the $-\hat{y}$ direction, the fork is now in the $-\hat{y}$ channel. Then, the current through each of the forks in the $-\hat{y}$ channel is $c_1\beta$, and the current through the $+\hat{y}$ channel is $\alpha + c_3\beta$. It is important to note that the constant parameters c_1, c_3 remain the same in both these cases. This is due to the symmetry of the $\pm\hat{y}$ directions with respect to the $+\hat{z}$ Zeeman field. Since the $\pm\hat{y}$ directions are indistinguishable with respect to the $+\hat{z}$-Zeeman field, the systems are also indistinguishable in the two cases and, thus, their constant parameters remain the same. Then, in the pres-

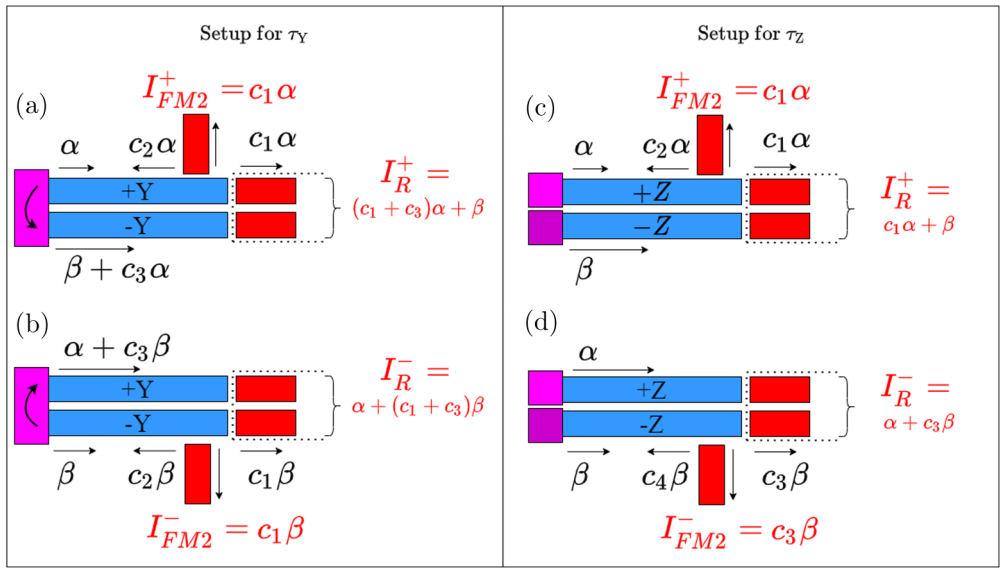

FIG. 8. (a) and (b) Schematics of the channel downstream of the barrier for the right polarized contact in $+\hat{y}$ and $-\hat{y}$ directions. Electrons that have tunneled through the barrier (pink) move along the two spin channels to the right where they are collected by the contacts (red). (c) and (d) Schematic of the channel downstream of the barrier for the right polarized contact in $+\hat{z}$ and $-\hat{z}$ directions. Note that unlike in (a) and (b), the barrier (pink) is now of different heights for the two spin channels.

ence of the ferromagnetic $-\hat{y}$-polarized contact, the currents through the two contacts are now given by $I^-_{FM2} = c_1\beta$ (for the $-\hat{y}$-polarized contact) and $I^-_R = (c_1 + c_3)\beta + \alpha$ (for the unpolarized contact).

To measure the polarization of the electron, we will now define a physically observable quantity called the signature of the electron, given by

$$D_Y = \frac{I^+_{FM2} - I^-_{FM2}}{I^+_{FM2} + I^-_{FM2}}, \tag{B1}$$

where $I^\pm_{FM2}$ is the current through the ferromagnetic contact whereas it is in the $\pm\hat{y}$ orientation, respectively.

This signature, is a measure of the spin polarization of the tunneled electron. In our simulations, it will play the same role as the quantity $\langle S_Y\rangle/(\hbar/2)$ defined by Büttiker [11]. Note that this is not the spin expectation value of the wave function in a particular direction. It is the Y-spin expectation value of the postselected part of the wave function.

It is easy to see that,

$$D_Y = \frac{I^+_{FM2} - I^-_{FM2}}{I^+_{FM2} + I^-_{FM2}} = \frac{(\alpha - \beta)}{(\alpha + \beta)}, \tag{B2}$$

which gives us back the polarization of spin in the $\hat{y}$ direction of the channel.

Then the weak value of the $\hat{y}$ spin of the electron is given by

$$\langle S_Y\rangle = (\hbar/2)\frac{I^+_{FM2} - I^-_{FM2}}{I^+_{FM2} + I^-_{FM2}} = -(\hbar/2)\omega_L\tau_Y. \tag{B3}$$

Thus, we have

$$\tau_Y = -\frac{1}{\omega_L}\frac{I^+_{FM2} - I^-_{FM2}}{I^+_{FM2} + I^-_{FM2}}. \tag{B4}$$

To measure the measurement backaction in this setup, the out-of-plane alignment of the spin polarization is to be measured. This is equivalent to a weak value measurement of the σ_Z operator. Thus, in this setup, the right ferromagnetic contact is polarized in the $\pm\hat{z}$ directions.

We refer to Figs. 8(c) and 8(d) for a description of the transport signal for τ_Z. Since we have to measure the polarization in the $\hat{z}$ direction, we now consider spin channels carrying electrons of spin polarizations $+\hat{z}$ and $-\hat{z}$. The primary difference to note here is that in this setup, the channels are not coupled to each other since the Zeeman field is in the $\hat{z}$ direction. As a result, the two setups corresponding to $\pm\hat{z}$-polarized ferromagnetic contact are nonidentical to each other.

Once again, let the currents through the two channels, in the absence of any forks be given by α and β, respectively, for the $\pm\hat{z}$ channels. Just as before, the presence of a fork in the $+\hat{z}$ channel then modifies the current through each of the forks to be $c_1\alpha$ where c_1 is some constant parameter (since the forks are identical). However, the current through the $-\hat{z}$ channel is unmodified in this case and simply β. Thus, in the presence of the ferromagnetic $+\hat{z}$-polarized contact, the currents through the two contacts are now given by $I^+_{FM2} = c_1\alpha$ (for the $+\hat{z}$-polarized contact) and $I^+_R = c_1\alpha + \beta$ (for the unpolarized contact).

Similarly, in the presence of the ferromagnetic $-\hat{z}$-polarized contact, the currents through the two contacts are now given by $I^-_{FM2} = c_3\beta$ (for the $+\hat{z}$-polarized contact) and $I^-_R = c_3\beta + \alpha$ (for the unpolarized contact).

Note that in this case, the constant parameters are not the same since the channels are no longer identical. However, we still need polarization of the form $(\alpha - \beta)/(\alpha + \beta)$. This can be realized with a different choice of signature given by

$$D_Z = \frac{(I^+_R - I^+_{FM2}) - (I^-_R - I^-_{FM2})}{(I^+_R - I^+_{FM2}) + (I^-_R - I^-_{FM2})}, \tag{B5}$$

where $I^{\pm}_{FM2}$'s are, as in the previous case, the current through the ferromagnetic contact whereas it is in the $\pm\hat{z}$ orientation, respectively. $I^{\pm}_{R}$ is the current through the right unpolarized contact when the ferromagnetic contact is in the $\pm\hat{z}$ orientation, respectively.

It is easy to see that $I^{+}_{R} - I^{+}_{FM2} = \beta$ and similarly, $I^{-}_{R} - I^{-}_{FM2} = \alpha$. Thus, we have

$$D_Z = -\frac{(I^{+}_{R} - I^{+}_{FM2}) - (I^{-}_{R} - I^{-}_{FM2})}{(I^{+}_{R} - I^{+}_{FM2}) + (I^{-}_{R} - I^{-}_{FM2})} = \frac{(\alpha - \beta)}{(\alpha + \beta)}. \tag{B6}$$

Then the weak value of the $\hat{z}$ spin of the electron is given by

$$\langle S_Z \rangle = -(\hbar/2)\frac{(I^{+}_{R} - I^{+}_{FM2}) - (I^{-}_{R} - I^{-}_{FM2})}{(I^{+}_{R} - I^{+}_{FM2}) + (I^{-}_{R} - I^{-}_{FM2})} = (\hbar/2)\omega_L \tau_Z. \tag{B7}$$

We then have

$$\tau_Z = -\frac{1}{\omega_L}\frac{(I^{+}_{R} - I^{+}_{FM2}) - (I^{-}_{R} - I^{-}_{FM2})}{(I^{+}_{R} - I^{+}_{FM2}) + (I^{-}_{R} - I^{-}_{FM2})}. \tag{B8}$$

It is also important to note that this choice of signature only holds true in the tunneling regime. When the particle is no longer tunneling, it is possible for the contact reflections to traverse back through the barrier and interact with the $+X$ contact which, in turn, couples the $\pm Z$ channels with each other. This violates our initial assumption that the current in the unforked channel is unaffected and, thus, distorts the results. In the tunneling regime, these reflections (which have to tunnel back through the barrier and then through it again) are of very low magnitude to cause any significant distortions in the result.

APPENDIX C: WEAK VALUES

When one tries to measure a variable attached to an operator, say $\hat{A}$, using a pointer generated via an operator, say $\hat{P}$, the generic interaction for the measurement within the von Neumann framework [19,20] is given by

$$\hat{H}_{\text{int}} = -g(t)\hat{P} \otimes \hat{A}. \tag{C1}$$

Here, $g(t)$ is a compact supported function in the duration of the measurement such that $\gamma = \int g(t)dt$ represents a small coupling parameter that characterizes this interaction. Based on the preselection and postselection, we can then characterize the measurement of an eigenvalue a_n of the operator $\hat{A}$ via the movement of the conjugate $\hat{Q}$ of the pointer variable $\hat{P}$, as derived quite explicitly in Ref. [17].

We need to measure the expectation of A, given the initial- and final-states $|i\rangle$ and $|f\rangle$. This is given as

$$\langle A \rangle_{fi} = \frac{\langle f|A||i\rangle}{\langle f|i\rangle}.$$

Let us assume that the pointer was initially in the state,

$$|\psi\rangle_i = \exp(-Q^2/4\sigma^2),$$

where σ^2 is the variance of Q. After the measurement, this then transforms to

$$\begin{aligned}|\psi\rangle_f &= \exp\left(\frac{-(Q - \langle A\rangle_{fi})^2}{4\sigma^2}\right) = \exp\left(\frac{-(Q - \mathrm{Re}\langle A\rangle_{fi} - i\,\mathrm{Im}\langle A\rangle_{fi})^2}{4\sigma^2}\right)\\ &= \exp\left(\frac{-(Q - \mathrm{Re}\langle A\rangle_{fi})^2}{4\sigma^2}\right)\exp\left(\frac{-(\mathrm{Im}\langle A\rangle_{fi})^2}{4\sigma^2}\right)\exp\left(\frac{-i\,\mathrm{Im}\langle A\rangle_{fi}(Q - \mathrm{Re}\langle A\rangle_{fi})}{2\sigma^2}\right).\end{aligned}$$

From the above, we see that the change in pointer position is given by

$$\Delta Q = \mathrm{Re}\langle A\rangle_{fi}, \tag{C2}$$

whereas the change in pointer momentum is the associated phase of the form $\exp(ipq)$ which means the change in pointer momentum,

$$\Delta P = \mathrm{Im}\langle A\rangle_{fi}/2\sigma^2, \tag{C3}$$

where ΔQ and ΔP are the weak values. However, this does not mean the measurement is weak. It becomes weaker when Q is more uncertain and, thus, σ increases as will be shown in the next part.

APPENDIX D: WEAK MEASUREMENTS IN OUR SETUP

In our setup, the pointer is ϕ and, therefore, the conjugate momentum is S_Z. The operator, whose expectation value needs to be measuredas shown by Steinberg [15], is $U(y) = 1/2[\Theta(y + L/2) - \Theta(y - L/2)]$, where $\Theta(y)$ is the Heaviside step function. Here the barrier is from $y = -L/2$ to $y = L/2$. To couple this operator to the pointer as in (1), we put a magnetic field inside the barrier in the Z direction. Thus, the Hamiltonian becomes

$$\hat{H} = -\gamma B_z \hat{S}_z \hat{U}(\hat{y}). \tag{D1}$$

Then, as shown in (C2) and (C3), the change in pointer position,

$$\Delta\phi = \omega_L \tau_Y = k\,\mathrm{Re}\langle U(y)\rangle_{fi}, \tag{D2}$$

where ω_L is the Larmor frequency. The change in pointer momentum,

$$\begin{aligned}\Delta S_Z = \omega_L \tau_Z &= k\,\mathrm{Im}\langle U(y)\rangle_{fi}/[2\,\mathrm{Var}(\phi)]\\ &= k\,\mathrm{Im}\langle U(y)\rangle_{fi} * \mathrm{Var}(S_Z)/2.\end{aligned} \tag{D3}$$

Since our initial state is in the $\hat{x}$-polarized direction, $\langle S_Z\rangle_i = 0 \Rightarrow \Delta S_Z = \langle S_Z\rangle_f - \langle S_Z\rangle_i = \langle S_Z\rangle_f$.

Thus, the pointer momentum measured by our device is indeed the correct and required change in pointer momentum.

However, this is not the case for ϕ. We are capable of measuring only the expectation value of spins of the electron and not the angle on the x-y plane. Specifically, this angle is the phase difference between the two components of the spinor. Consider a spinor of the form

$$|\psi\rangle = \begin{bmatrix} \cos\theta/2 \\ \sin\theta/2\, e^{i\phi} \end{bmatrix},$$

$$\text{then, } \langle\psi|S_Y|\psi\rangle = 2\sin(\theta/2)\cos(\theta/2)\sin\phi = \sin\phi\sin\theta. \tag{D4}$$

If our spinor is initially in state $\theta = \pi/2$, we have

$$\langle\psi|S_Y|\psi\rangle = \sin\phi \approx \phi \text{ when } \phi \to 0.$$

Thus, we can obtain the change in ϕ via the measurement of S_Y only when ϕ is very small. Now we need to find ϕ in the case where $\theta \neq \pi/2$. Note that

$$\langle\psi|S_Z|\psi\rangle = \cos^2\theta/2 - \sin^2\theta/2. \tag{D5}$$

Then the variance in S_Z,

$$\text{Var}(S_Z) = 1 - \langle S_Z\rangle^2 = 1 - \cos^2\theta = \sin^2\theta. \tag{D6}$$

Combining (D4) and (D6), we have

$$\frac{\langle\psi|S_Y|\psi\rangle}{\sqrt{\text{Var}(S_Z)}} = \sin\phi \approx \phi \text{ when } \phi \to 0. \tag{D7}$$

From (D2), we know that $\Delta\phi$ should remain constant even when $\text{Var}(\phi)$ changes. Thus, from (D7), we see that $\frac{\langle\psi|S_Y|\psi\rangle}{\sqrt{\text{Var}(S_Z)}}$ must remain constant and this is verified using NEGF.

Similarly, from (D3), we see that $\Delta S_Z * \text{Var}(\phi)$ must remain constant which means, $\Delta S_Z/\text{Var}(S_Z)$ must remain constant as is quite well verified using our NEGF approach also.

Thus, we see that the measurement can be made weaker by changing the polarization of the electron to $\phi < \pi/2$. This decreases the uncertainty in S_Z and, therefore, increases the uncertainty in ϕ. The measurement backaction, ΔS_Z is found to decrease proportionally to the decrease in $\text{Var}(S_Z)$. The real part of the measurement ϕ remains a constant, but since that cannot be explicitly measured, we show that the measured quantity, $\langle\psi|S_Y|\psi\rangle$ decreases proportionally to the square root of $\text{Var}(S_Z)$ and that $\phi = \frac{\langle\psi|S_Y|\psi\rangle}{\sqrt{\text{Var}(S_Z)}}$ is the actual real part of the measurement.

[1] J. Leon and L. Maccone, Found. Phys. **47**, 1597 (2017).
[2] H. Salecker and E. P. Wigner, Phys. Rev. **109**, 571 (1958).
[3] A. Peres, Am. J. Phys. **48**, 552 (1980).
[4] Y. Choi and A. N. Jordan, Phys. Rev. A **88**, 052128 (2013).
[5] R. Landauer and T. Martin, Rev. Mod. Phys. **66**, 217 (1994).
[6] H. G. Winful, Phys. Rev. Lett. **90**, 023901 (2003).
[7] H. G. Winful, Phys. Rep. **436**, 1 (2006).
[8] A. G. Kofman, S. Ashhab, and F. Nori, Phys. Rep. **520**, 43 (2012), nonperturbative theory of weak pre- and post-selected measurements.
[9] U. S. Sainadh, R. T. Sang, and I. V. Litvinyuk, J. Phys. Photonics **2**, 042002 (2020).
[10] M. Büttiker and R. Landauer, Phys. Rev. Lett. **49**, 1739 (1982).
[11] M. Büttiker, Phys. Rev. B **27**, 6178 (1983).
[12] A. I. Baz', Sov. J. Nucl. Phys. **4**, 182 (1967).
[13] A. I. Baz', Sov. J. Nucl. Phys. **5**, 161 (1967).
[14] V. F. Rybachenko, Sov. J. Nucl. Phys. **5**, 635 (1967).
[15] A. M. Steinberg, Phys. Rev. Lett. **74**, 2405 (1995).
[16] Y. Aharonov, D. Z. Albert, and L. Vaidman, Phys. Rev. Lett. **60**, 1351 (1988).
[17] I. M. Duck, P. M. Stevenson, and E. C. G. Sudarshan, Phys. Rev. D **40**, 2112 (1989).
[18] Y. Aharonov and L. Vaidman, Phys. Rev. A **41**, 11 (1990).
[19] B. Tamir and E. Cohen, Quanta **2**, 7 (2013).
[20] J. Dressel and A. N. Jordan, Phys. Rev. Lett. **109**, 230402 (2012).
[21] J. Dressel, M. Malik, F. M. Miatto, A. N. Jordan, and R. W. Boyd, Rev. Mod. Phys. **86**, 307 (2014).
[22] R. Ramos, D. Spierings, I. Racicot, and A. M. Steinberg, Nature (London) **583**, 529 (2020).
[23] D. C. Spierings and A. M. Steinberg, Phys. Rev. Lett. **127**, 133001 (2021).
[24] Igor Žutić, J. Fabian, and S. Das Sarma, Rev. Mod. Phys. **76**, 323 (2004).
[25] A. Fert and F. N. Van Dau, C. R. Phys. **20**, 817 (2019).
[26] A. Hirohata, K. Yamada, Y. Nakatani, I.-L. Prejbeanu, B. Diény, P. Pirro, and B. Hillebrands, J. Magn. Magn. Mater. **509**, 166711 (2020).
[27] S. Datta, *Electronic Transport in Mesoscopic Systems* (Cambridge University Press, Cambridge, UK, 1997)
[28] Y. Meir and N. S. Wingreen, Phys. Rev. Lett. **68**, 2512 (1992).
[29] H. Haug and A. Jauho, *Quantum Kinetics in Transport and Optics of Semiconductors*, Springer Series in Solid-State Sciences (Springer, Berlin/Heidelberg, 2007).
[30] P. Danielewicz, Ann. Phys. (NY) **152**, 239 (1984).
[31] R. Golizadeh-Mojarad and S. Datta, Phys. Rev. B **75**, 081301(R) (2007).
[32] A. Sharma, A. Tulapurkar, and B. Muralidharan, IEEE Trans. Electron Devices **63**, 4527 (2016).
[33] A. Sharma, A. A. Tulapurkar, and B. Muralidharan, Appl. Phys. Lett. **112**, 192404 (2018).
[34] A. Singha and B. Muralidharan, J. Appl. Phys. **124**, 144901 (2018).
[35] A. Sharma, A. A. Tulapurkar, and B. Muralidharan, Phys. Rev. Appl. **8**, 064014 (2017).
[36] K. Y. Camsari, S. Chowdhury, and S. Datta, The non-equilibrium green function (negf) method (2020), arXiv:2008.01275 [Spinger Handbook of Semiconductor Devices (to be published)].
[37] C. Duse, P. Sriram, K. Gharavi, J. Baugh, and B. Muralidharan, J. Phys.: Condens. Matter **33**, 365301 (2021).
[38] Y. Niimi, Y. Kawanishi, D. H. Wei, C. Deranlot, H. X. Yang, M. Chshiev, T. Valet, A. Fert, and Y. Otani, Phys. Rev. Lett. **109**, 156602 (2012).
[39] A. Lahiri, K. Gharavi, J. Baugh, and B. Muralidharan, Phys. Rev. B **98**, 125417 (2018).
[40] A. Basak, P. Brahma, and B. Muralidharan, J. Phys. D: Appl. Phys. **55**, 075302 (2022).
[41] K. Jana and B. Muralidharan, npj 2D Mater. Appl. **6**, 19 (2022).

[42] A. A. Yanik, G. Klimeck, and S. Datta, Phys. Rev. B **76**, 045213 (2007).
[43] I. Appelbaum, B. Huang, and D. J. Monsma, Nature (London) **447**, 295 (2007).
[44] M. Wu, J. Jiang, and M. Weng, Phys. Rep. **493**, 61 (2010).
[45] P. Erker, M. T. Mitchison, R. Silva, M. P. Woods, N. Brunner, and M. Huber, Phys. Rev. X **7**, 031022 (2017).
[46] M. Gopalkrishnan, V. Kandula, P. Sriram, A. Deshpande, and B. Muralidharan, Phys. Rev. A **96**, 032339 (2017).
[47] A. N. Pearson, Y. Guryanova, P. Erker, E. A. Laird, G. A. D. Briggs, M. Huber, and N. Ares, Phys. Rev. X **11**, 021029 (2021).
[48] A. Singha, M. H. Fauzi, Y. Hirayama, and B. Muralidharan, Phys. Rev. B **95**, 115416 (2017).
[49] M. H. Fauzi, A. Singha, M. F. Sahdan, M. Takahashi, K. Sato, K. Nagase, B. Muralidharan, and Y. Hirayama, Phys. Rev. B **95**, 241404(R) (2017).
[50] M. H. Fauzi, M. F. Sahdan, M. Takahashi, A. Basak, K. Sato, K. Nagase, B. Muralidharan, and Y. Hirayama, Phys. Rev. B **100**, 241301(R) (2019).
[51] S. Datta and B. Das, Appl. Phys. Lett. **56**, 665 (1990).
[52] A. R. H. Smith and M. Ahmadi, Nat. Commun. **11**, 5360 (2020).